Non-topotactic reactions enable high rate in Li-rich cathode materials

Jianping Huang[1], Peichen Zhong[1,2], Yang Ha[3], Deok-Hwang Kwon[1,2], Matthew J. Crafton[4], Yaosen Tian[1,2], Mahalingam Balasubramanian[5], Bryan D. McCloskey[4,6], Wanli Yang[3], Gerbrand Ceder[1,2*]

1 Materials Sciences Division, Lawrence Berkeley National Laboratory, Berkeley, CA, USA

2 Department of Materials Science and Engineering, University of California, Berkeley, CA, USA

3 Advanced Light Source, Lawrence Berkeley National Laboratory, Berkeley, CA 94720, USA

4 Department of Chemical and Biomolecular Engineering, UC Berkeley, Berkeley, CA 94720, USA

5 X-ray Science Division, Advanced Photon Source, Argonne National Laboratory, Argonne, IL, USA

6 Energy Storage and Distributed Resources Division, LBNL, Berkeley, CA 94720, USA

*Correspondence to: gceder@berkeley.edu

Abstract

High-rate cathode materials for Li-ion batteries require fast Li-transport kinetics, which typically relies on topotactic Li intercalation/de-intercalation because it minimally disrupts Li-transport pathways. In contrast to this conventional view, herein, we demonstrate that the rate capability in a Li-rich cation-disordered rocksalt (DRX) cathode can be significantly improved when the topotactic reaction is replaced by a non-topotactic reaction. The fast non-topotactic lithiation reaction is enabled by facile and reversible transition-metal (TM) octahedral-to-tetrahedral migration, which improves rather than impedes Li transport. Using this concept, we show that high-rate performance can be achieved in Mn- and Ni-based DRX materials when some of the TM content can reversibly switch between octahedral and tetrahedral sites. This study provides a new perspective on the design of high-performance cathode materials by demonstrating how the interplay between Li and TM migration in materials can be conducive to fast non-topotactic Li intercalation/de-intercalations.

Main

The need for novel ideas for Li-ion batteries with high energy and high power is becoming increasingly important as society enters a new electrified era. The operation of a Li-ion battery requires the shuttling of Li^+ ions in and out of electrode materials. To support fast Li transport, a perfect topotactic reaction, whereby the host material remains unchanged as its Li content changes, is generally considered crucial because of the minimal disruption to Li-transport pathways.[1,2] A topotactic reaction involves reversible Li intercalation into the host structure with only lattice parameter and bond length changes, but does not involve diffusive rearrangement of the host atoms.[3,4] In some electrode materials with large capacity, transport of other ionic species besides Li can also occur, leading to a change in the material's structure[5,6]. The transport of multiple ionic species not only increases the kinetic complexities but also affects the Li-transport pathways, which is why such non-topotactic reactions are usually not sought out. For example, a large mismatch in the ionic mobilities of the Li and other mobile ionic species can lead to voltage hysteresis.[7] In conversion-type electrode materials (e.g., FeF_2, CuF_2, FeOF, Fe_3O_4), sluggish transition-metal (TM) or anion migration limits the redox reaction kinetics and induces voltage hysteresis >1 V.[6,8,9]

The non-topotactic phenomenon is also observed in some intercalation-type electrode materials when TM cations have some mobility. For example, voltage relaxation from 5.2 to 4.5 V occurs in layered $LiNi_{0.5}Mn_{0.5}O_2$ at the top of charge because of sluggish Ni migration, and the slow TM motion limits the usable amount of Li that can be inserted at low voltages, thereby resulting in poor rate performance.[10,11] Similarly, poor electrochemical performance in layered $LiCrO_2$ has been attributed to blocked Li diffusion because of Cr migration, even though $LiCrO_2$ shows a high degree of structural similarity to $LiCoO_2$, an extensively commercialized battery electrode

material.[12,13] Hence, a general design principle for high-power cathode materials has been to pursue a perfect topotactic reaction to maintain the structural framework and minimize kinetic complexities. $LiFePO_4$ and spinel $LiMn_2O_4$ are successful examples of this approach. This strategy may have come to an end as the only cations that have virtually no mobility in dense oxides are those used in the currently used NMC layered oxides, and discovery of new large-capacity cathode materials will require one to manage the mobility of the non-working cations. While polyanion systems are generally better at fixing a metal in place, they tend to have low energy density, and as such are unlikely to spur further energy density improvements.

In this paper, we present an example where the Li-transport kinetics can be greatly improved when a topotactic reaction is replaced by a non-topotactic reaction, indicating that focus on fully topotactic intercalation may have led the field to overlook some opportunities for cathode design. We show that in the DRX $Li_{1.2}Mn_{0.2}Ti_{0.4}Cr_{0.2}O_2$ fast Li transport is enabled by facile and reversible Cr octahedral-to-tetrahedral migration at the top of charge which creates new paths for Li migration. Li-rich cation-disordered rocksalt (DRX) materials possess a face-centered-cubic (fcc) anion framework with Li transport occurring through a percolation network of Li-rich tetrahedral environments (0-TM channels, where the tetrahedral site does not face-share with any TM).[14,15] As Li percolation is supported by the connectivity of available tetrahedral 0-TM channels, any TM occupancy in the tetrahedral site can potentially disrupt such connectivity, and TM migration in DRX materials can be detrimental to Li transport. Surprisingly, we observe that cation-disordered $Li_{1.2}Mn_{0.2}Ti_{0.4}Cr_{0.2}O_2$, where most of the Cr has migrated to tetrahedral sites at the top of charge (TOC), shows significantly improved rate performance (40% vs. 57% capacity reduction when increasing rate from 20 to 1000 mA g^{-1}) relative to $Li_{1.2}Mn_{0.4}Ti_{0.4}O_2$ which has no tetrahedral TM upon charging. We demonstrate that the subtle change in the Cr coordination environment

redefines the 0-TM Li percolation network at the TOC and increases the percolating Li content, contributing to the high-rate performance. To prove the generalizability of this TM migration concept, we also applied the Cr substitution to a Ni-based DRX system and similarly achieved a significant increase in rate performance (160 mAh g^{-1} delivered in 10 min). In contrast to the conventional view of TM migration, our results suggest that the appropriate use of facile TM migration is promising for the design of high-performance cathode materials.

Characterization and electrochemistry of $Li_{1.2}Mn_{0.4-x}Ti_{0.4}Cr_xO_2$

Cation-disordered $Li_{1.2}Mn_{0.4}Ti_{0.4}O_2$ (LMTO), $Li_{1.2}Mn_{0.3}Ti_{0.4}Cr_{0.1}O_2$ (LMTC01O), and $Li_{1.2}Mn_{0.2}Ti_{0.4}Cr_{0.2}O_2$ (LMTC02O) were synthesized using a solid-state method. The X-ray diffraction (XRD) patterns of the three samples can be indexed to a disordered rocksalt phase (Fm-3m) without any apparent impurity peaks, Fig. 1a. The Rietveld refinement results indicate that the lattice constant decreases from 4.1530 to 4.1480 and 4.1420 Å with increasing Cr substitution, consistent with the smaller ionic radius of Cr^{3+} than Mn^{3+}. The scanning transmission electron microscope (STEM)/energy-dispersive X-ray spectroscopy (EDS) mappings show that elements are uniformly distributed in LMTO (Fig. 1b, Mn, Ti, and O) and LMTC02O (Fig. 1c, Mn, Ti, Cr, and O). The as-prepared materials were shaker-milled for the electrochemical measurements. Scanning electron microscopy (SEM) images reveal similar particle sizes ranging from 130 to 200 nm in the three samples, Fig. 1d.

Galvanostatic cycling at 20 mA g^{-1} between 1.5 and 4.8 V indicates that the $Li_{1.2}Mn_{0.4-x}Ti_{0.4}Cr_xO_2$ samples have similar initial charge and discharge capacities, Fig. 2a and 2b and Supplementary Fig. 1. LMTO and LMTC02O deliver discharge capacities (energy densities) of 253 (786 Wh kg^{-1}) and 257 mAh g^{-1} (790 Wh kg^{-1}), respectively. Upon increasing the current density from 20 to 1000 mA g^{-1}, the initial discharge capacity of LMTO decreases to 109 mAh g^{-1} at 1000 mA g^{-1}.

In contrast, the initial discharge capacity of LMTC02O remains at 155 mAh g^{-1} at 1000 mA g^{-1}. The higher rate capability of LMTC02O is also observed for subsequent cycles (Supplementary Fig. 2). In the voltage window of 4.1–1.5 V, LMTC02O still maintains better rate capability than LMTO (Supplementary Fig. 3).

Galvanostatic intermittent titration technique (GITT) measurements were used to probe the Li kinetics in $Li_{1.2}Mn_{0.4-x}Ti_{0.4}Cr_xO_2$. The quasi-equilibrium voltage profiles of LMTO and LMTC02O do not display large hysteresis (Supplementary Fig. 4). The apparent Li diffusion coefficient was determined by determining the chemical diffusion coefficient from the GITT and dividing it by the thermodynamic enhancement factor (Supplementary Note 1, Supplementary Fig. 5). As the Li content is reduced from $Li_{1.2}TM_{0.8}O_2$ to $Li_{0.6}TM_{0.8}O_2$, LMTO and LMTC02O maintain similar Li diffusion coefficients of 2–4 × 10^{-16} cm^2 s^{-1}, Fig. 2f. However, the apparent Li diffusion coefficient of LMTO decreases by one order of magnitude when more than 0.6 Li per $Li_{1.2}TM_{0.8}O_2$ formula unit (f.u.) is extracted while such a decrease is not observed in LMTC02O upon charging. Approximately 1 Li per f.u. can be extracted with a reasonable Li diffusion coefficient (>2 × 10^{-16} cm^2 s^{-1}) from LMTC02O indicating improved Li kinetics of LMTC02O relative to that of LMTO at the TOC. The improved Li kinetics of LMTC02O upon charging contributes to its improved rate performance relative to LMTO, which is further supported by electrochemical impedance spectroscopy (Supplementary Note 2, Supplementary Fig. 6) and cyclic voltammetry (Supplementary Note 3, Supplementary Fig. 7) results. Note that the actual diffusion coefficient depends on an approximation for the active surface area, however this uncertainty does not affect the relative variations with Li content.

Redox mechanism and structural change

Hard X-ray absorption spectroscopy (XAS) and soft X-ray mapping of resonant inelastic X-ray scattering (mRIXS) were used to analyze the TM and oxygen redox in LMTO and LMTC02O, respectively, Fig. 3a–3e. Mn K-edge X-ray absorption near edge structure (XANES) spectra reveal that both LMTO and LMTC02O undergo Mn^{3+}/Mn^{4+} oxidation when charged to 4.8 V (Fig. 3a and 3b). Upon discharging to 1.5 V, the XANES spectra of LMTO and LMTC02O almost recover to those of the pristine states, indicative of the reduction of Mn^{4+} to Mn^{3+}. A prominent pre-edge component in the Cr K-edge XANES is a characteristic feature of Cr^{6+}, which is attributed to a 1s → 3d transition. Comparison of the pre-edge intensities in the Cr K-edge XANES spectra[16] of the CrO_3 standard and the 4.8-V-charged LMTC02O provides strong evidence that Cr^{3+} in LMTC02O is fully oxidized to Cr^{6+} (Fig. 3c). The prominent pre-edge feature disappears as LMTC02O is discharged to 1.5 V, indicating that the Cr^{3+}/Cr^{6+} redox is mostly reversible. Ti K-edge XANES indicates that Ti^{4+} in LMTO and LMTC02O is not redox-active within the applied voltage window (Supplementary Fig. 8).

The oxidation of lattice oxygen was probed using O K-edge mRIXS, which has been shown to be a robust technique in detecting the oxidized lattice oxygen in battery cathodes[17,18]. It has been established in many oxygen redox systems that an mRIXS feature around 531 eV excitation and 523.7 eV emission energies will emerge when the electrode is charged, indicating oxidized oxygen in the charged state[17,18]. Indeed, the O K-edge mRIXS shows this characteristic feature of oxidized lattice oxygen in the 4.8-V-charged LMTO (Fig. 3d) and 4.8-V-charged LMTC02O (Fig. 3e), indicating the oxidation of lattice oxygen upon charging. Differential electrochemical mass spectrometry (DEMS) analysis revealed minor O_2 gas evolution upon charging in both LMTO and LMTC02O, suggesting a small amount of irreversible oxygen oxidation (Supplementary Fig. 9). This O-release is common in DRX cathodes but is generally smaller than in high Ni layered

cathodes[19,20]. The observed CO_2 evolution may originate from the oxidation of residual lithium carbonate or the carbonate solvents, as shown in prior literature[21,22].

The ex-situ XRD patterns indicate that the bulk structural change in LMTO and LMTC02O is reversible upon charging and discharging (Supplementary Fig. 10). The lattice constants only decrease by 1.4% (LMTO) and 1.0% (LMTC02O) after charging to 4.8 V and almost recover to those of the pristine state after discharging to 1.5 V, reiterating the very small volume changes seen in some DRX materials[14,15]. The local structural changes were characterized using extended X-ray absorption fine structure (EXAFS) spectroscopy. In the Cr K-edge EXAFS spectra, the peaks at ~1.0, ~1.5, and ~2.5 Å correspond to the tetrahedral Cr–O ($Cr–O_{tet}$), octahedral Cr–O ($Cr–O_{oct}$), and Cr–TM coordination, respectively. The EXAFS fitting reveals that in the pristine state of LMTC02O all the Cr resides in octahedral sites (Cr_{oct}) with a Cr–O bond distance of ~1.98 Å (Fig. 3f, Supplementary Table 1). The majority of Cr (99±9%) migrated to tetrahedral sites (Cr_{tet}) in the 4.8-V-charged state, and the Cr–O bond distance decreased to ~1.63 Å. Most of the tetrahedral Cr reversibly migrated back to the octahedral sites upon discharging to 1.5 V (Supplementary Note 4, Supplementary Fig. 11). The occupation of Mn and Ti in the tetrahedral sites was not observed in LMTO or LMTC02O (Supplementary Fig. 12), confirming that Mn^{3+} (Mn^{4+}) and Ti^{4+} prefer the octahedral sites.

Discussion

Li diffusion in rocksalt-like oxides occurs by oct-tet-oct jumps[23,24]. While in layered cathode materials these Li jumps are confined to the two-dimensional Li slab, in DRX materials they occur through the statistically percolating network of tetrahedral sites that have no face-sharing TM (0-TM).[14,25] Thus, an increase in the amount and connectivity of 0-TM tetrahedra is conducive to improving the Li kinetics in DRX materials. Fig. 4a illustrates how occupation of an octahedral

site by a TM inhibits Li migration through the eight tetrahedral sites it shares a face with. If this octahedral TM moves into a neighboring tetrahedral site (Fig. 4b) it creates seven potential new 0-TM channels, depending on the occupancy of the other octahedra these tetrahedra face-share with. Specific conditions are required for a TM to migrate to a tetrahedral site: 1) A tetrahedral site can only be occupied when its face-sharing octahedral sites are empty, which is more likely near the TOC where Li tri-vacancies can form. 2) The TM has to prefer 4-fold over 6-fold coordination, which is determined by its electronic structure and size[26]. As shown by the XAS results, Cr^{6+} forms in the charged state, which, with its d^0 electronic configuration and small ionic radius in the tetrahedral site (0.26 Å according to Shannon[27]) is likely to favor the tetrahedral site. The tri-vacancy condition for the migration event allow us to partially characterize the environment of the tetrahedral sites around the octahedral site that is vacated by TM migration as shown in Fig. 4b. Three of the tetrahedra face-share with at least two octahedral vacancies (2-V_a tetrahedra, green circles in Fig. 4b), and four tetrahedra have one octahedral vacancy guaranteed (1-V_a tetrahedra, yellow circles in Fig. 4b). The 2-V_a and 1-V_a tetrahedra become 0-TM channels if the other face-sharing octahedral sites are occupied by a Li (or vacancy at later stages of delithiation). As sixty percent of the octahedral sites are occupied by Li in $Li_{1.2}TM_{0.8}O_2$, the 2-V_a tetrahedra have a 36% (0.6×0.6) possibility of being a 0-TM channel, and the 1-V_a tetrahedra have a 21.6% (0.6×0.6×0.6) possibility of being a 0-TM channel, assuming a random cation distribution. Therefore, Cr migration will generate on average ≈2 (0.36×3+0.216×4) new 0-TM channels out of the eight tetrahedral sites. This demonstration shows that TM octahedral–to–tetrahedral (oct–tet) migration in a disordered rocksalt-type structure is likely to create additional Li transport pathways, leading to better Li kinetics.

In an actual DRX material, cation short-range order (SRO) affects the overall cation distribution, which determines the amount and connectivity of the 0-TM channels.[28] To model such a more realistic condition, we performed cluster-expansion Monte Carlo (MC) simulations to investigate the changes in Li percolation by Cr oct–tet migration in the presence of SRO, Fig. 4c and 4d. MC simulation was performed at 1273 K, with 1000 MC representative structures sampled from the equilibrium ensemble. In the pristine (discharged) state ~36% Li were found to be part of the 0-TM percolating network in LMTC02O, about the same as for LMTO[28]. To reveal how Cr migration modifies the percolating Li content, we first investigated whether Cr migration is energetically favorable upon delithiation. We compared the energies of Cr_{oct} and Cr_{tet} in the presence of a tri-Li vacancy, as described in the Methods section, and find that migration of Cr to the tetrahedral sites lowers the energy by ~0.3 eV with reasonable migration barriers (Supplementary Note 5, Supplementary Fig. 13), indicating feasible Cr migration to the tetrahedral site. We found that in the MC configurations sampled at 1273 K 87% of the Cr was in an environment where it would be able to migrate to a near-neighbor tetrahedral site upon delithiation in LMTC02O. As a result of this migration, ~80% of the Li sites become part of the 0-TM network, which more than doubles the amount of Li that is part of the percolating migration path. Overall, it is remarkable how this subtle change in the Cr coordination environment redefines the Li percolation network, leading to improved Li kinetics.

Extension to other systems

To verify the generalizability of this concept to other DRX materials, we also studied a Ni-based system by comparing the rate behavior of cation-disordered $Li_{1.2}Ni_{0.2}Ti_{0.6}O_2$ (LNTO) with that of $Li_{1.2}Ni_{0.1}Ti_{0.5}Cr_{0.2}O_2$ (LNTC02O). The XRD patterns and TEM results indicate that Cr could be successfully introduced into the bulk structure of LNTC02O, Fig. 5a and 5b and Supplementary

Fig. 14. The rate performance of the Cr substituted sample is considerably higher than that of the non-substituted sample, even though the amount of Ni redox is decreased. Whereas $Li_{1.2}Ni_{0.2}Ti_{0.6}O_2$ (LNTO) only retains 30% of its capacity (216 to 64 mAh g^{-1}) upon increasing the current density from 20 to 1000 mA g^{-1}, LNTC02O retains 60% (271 to 160 mAh g^{-1}) for the same current increase (Fig 5c). Upon electrochemical cycling at 1000 mA g^{-1}, LNTC02O maintains a reversible capacity of 110 mAh g^{-1} for 100 cycles, Fig. 5d. In the voltage window of 4.3–1.5 V, the $Li_{1.2}Ni_{0.2-x}Ti_{0.6-x}Cr_{2x}O_2$ samples all showed reasonable capacity retention with <0.3% capacity fade per cycle, and LNTC02O maintained a capacity >184 mAh g^{-1} for 50 cycles at 20 mA g^{-1} (Supplementary Fig. 15). The apparent Li diffusion coefficients, determined from GITT (Supplementary Fig. 16), indicate similar Li kinetics in LNTO and LNTC02O during the initial delithiation process (x in $Li_{1.2-x}TM_{0.8}O_2$ is <0.3), Fig. 5e. When more Li is removed, the diffusion coefficient in LNTO continuously decreases to ~1×10^{-17} cm^2 s^{-1} whereas diffusivity of lithium in LNTC02O remains at ~1×10^{-16} cm^2 s^{-1} for the full range of 1 Li^+ per f.u. extraction. The faster Li kinetics of LNTC02O in the highly delithiated state can be attributed to the formation of tetrahedral Cr^{6+} during the charge process (Fig. 5f, Supplementary Note 6 for the redox mechanism, Supplementary Fig. 17–19), consistent with that of the Cr-substituted Mn-based samples. RIXS spectra also reveal oxygen oxidation in both the LNTO and LNTC02O samples, as evidenced by the peak at the emission energy of 523.7 eV[17] (Fig. 5g, Supplementary Fig. 18). The peak feature of oxidized oxygen disappeared when LNTO/LNTC02O was discharged to 1.5 V, indicating a reversible reduction of the oxidized oxygen.

We believe that this non-topotactic behavior is also responsible for the reported performance of some other DRX materials. A relatively low percolating Li content (<15%) has been predicted in some V-based DRX materials ($Li_{1.2}V_{0.6}Nb_{0.2}O_2$ and $Li_{1.2}V_{0.67}Mo_{0.13}O_2$)[28], somewhat inconsistent

with the good performance of these materials as disordered $Li_{1.25}V_{0.5}Nb_{0.25}O_2$[29] delivers initial charge/discharge capacities of 250 mAh g^{-1}, corresponding to 67% Li utilization. The prominent pre-edge feature in the V K-edge XANES spectra[29] implies the presence of tetrahedral V^{5+} in the charged state, although detailed V–O bond analyses (for example, V K-edge EXAFS) would be required to unambiguously confirm this. But it appears likely that, as in the Cr-doped systems, V^{5+} migration to tetrahedral sites improves the Li diffusion network and hence the kinetics of this material as it is being charged.

Our experimental and theoretical results indicate that non-topotactic delithiation can improve the Li kinetics. The rate performance of both Mn and Ni redox based DRX materials is significantly improved by the addition of Cr. Further support for the benefits of Cr migration on the Li kinetics is the lack of any drop in the measured Li diffusivity in the Cr-doped samples, whereas undoped samples see reduced diffusivity after about 100 mAh g^{-1} (LNTO) and 200 mAh g^{-1} (LMTO). These results are consistent with the ab-initio computed driving force for Cr to migrate to tetrahedral sites near the TOC, and the geometric analysis showing that TM migration produces an increase in lithium pathways. The rate performance of the Cr-doped materials is comparable to that of state-of-the-art Li-rich cathodes, such as doped $Li_{1.2}Ni_{0.2}Mn_{0.6}O_2$, Li-rich NMC, and Li_2RuO_3-based materials (Supplementary Table 2)[30–33] despite the presence of oxygen oxidation (RIXS results). Some recent studies on Li-rich layered cathodes have shown that the oxidized oxygen species are stabilized by metal–oxygen decoordination, which requires TM migration.[34] It is possible that the Cr oct–tet migration in DRX materials creates such metal–oxygen decoordination, thereby limiting its ability to degrade the rate.

Our results may force a rethinking of the conventional view that TM migration is an unfavorable phenomenon that impedes Li transport and increases hysteresis[7–10]. We now discuss in more detail

the specific requirements for non-topotactic changes to improve kinetics, first with specific focus on the Cr-doped DRX systems, and then in a broader, more general context of cathode materials. The transition metal is the main obstacle for the diffusion of Li as its electrostatic repulsion dominates the energy in the activated state[23,24,35]. From this perspective, displacement of some transition metals to tetrahedral sites is obviously favorable as it clears multiple oct-tet-oct paths from neighboring transition metals, lowering the barrier for lithium to migrate through them, as our analysis in Fig. 4b shows. Migration of a TM from an octahedral to a tetrahedral site is enabled by an appropriate electronic configuration and ionic size. While d^3-Cr^{3+} has a strong preference for octahedral occupancy, the oxidized d^0-Cr^{6+} has no ligand field stabilization in the octahedral site. Other electronic configurations, such as d^5 and d^{10} are also favorable for TM migration to the tetrahedral site[26]. Another contributing factor for facile TM migration is the match between the TM size and the tetrahedron height. For example, a tetrahedron height of 2.39 Å (centroid–vertex distance of 1.79 Å) is large enough for a tetrahedral Cr–O bond (1.64 Å[27]) but too small for a tetrahedral Ti–O bond (1.80 Å[27]). As a result, d^0-Cr^{6+} migrates to the tetrahedral site while d^0-Ti^{4+} remains octahedral. In some layered cathodes with larger tetrahedron height (~2.56 Å), oct–tet migration of Ti^{4+} does occur[36] showing that both the requirements for the electronic configuration and ionic size need to be satisfied to enable TM migration.

While our focus has been on non-topotactic Li-cycling in DRX materials, we highlight a set of more general conditions that may have to be satisfied in order for non-topotactic behavior not to impede transport. 1) The non-topotactic processes should be fast and reversible. Slow processes will cause hysteresis which reduces the discharge energy. As only a few atomic hops may be required for the non-topotactic process, atomic migration processes with activation barrier below 1eV are relevant. In our example of Cr-substituted DRX materials, a single hop from an octahedral

site to a tetrahedral site is all that is needed to improve Li kinetics. 2) If possible, the non-topotactic processes should be non-cooperative. Large-scale coordinated processes tend to have a high activation energy and almost certainly will lead to hysteresis. This requirement exemplifies one advantage of DRX materials. Because of their disordered nature the oct-tet TM migration at a specific site occurs independently of the migration at other sites, creating essentially a set of randomly oriented strain dipoles. This is in stark contrast with layered materials that have oct-tet migration, such as $LiCrO_2$,[13] where preferential migration of Cr into the tetrahedral site in the Li layer creates a much more cooperative transition.

It may be possible to also improve layered oxides by enabling non-topotactic phenomena. Near the TOC layered materials experience a large contraction of slab spacing which reduces the Li mobility. The presence of other cations in the slab can mitigate this contraction by acting as a "pillar" and increase Li mobility at TOC. However, in the discharged state small high-valent ions usually contract the slab space too much, reducing the discharge kinetics. The difference in performance this leads to can for example be seen by comparing solid-state synthesized $Li(Ni_{0.5}Mn_{0.5})O_2$ which has considerable Ni in the Li slab, with ion-exchanged $Li(Ni_{0.5}Mn_{0.5})O_2$[1,10,37], which has almost no Ni in the Li layer. An ion that would move to the Li-slab at TOC and move back into the TM layer at the end of discharge would improve kinetics at both charge and discharge. Other non-topotactic, but reversible metal migrations, have been observed in Mg intercalation electrochemistry.[38] While the use of Cr in commercial cathodes may raise some issues concerning its strong oxidizing character and toxicity, appropriate engineering controls at electrode/cell level (e.g. surface coating and battery recycling) should help reduce these potential hazards similar to those implemented in the lead-acid battery industry. In addition, it may

be possible to mimic the Cr effect with other transition metals (e.g. V^{5+}, Mo^{6+}, Fe^{3+}, and Mn^{2+}) that can undergo octahedral-to-tetrahedral migration.

In conclusion, we demonstrated significantly improved rate performance in cation-disordered rocksalt cathodes due to a non-topotactic reaction, which is in contrast to the conventional view that fast Li transport is favored by perfectly topotactic systems. In our example, the fast non-topotactic reaction is enabled by reversible TM migration between the oct and tet site which improves the Li diffusion network by creating additional Li-transport pathways. We believe that well engineered non-topotacticity is a new opportunity to design high capacity cathode materials.

Methods

Synthesis. $Li_{1.2}Mn_{0.4-x}Ti_{0.4}Cr_xO_2$ and $Li_{1.2}Ni_{0.2-x}Ti_{0.6-x}Cr_{2x}O_2$ were synthesized using a solid-state method. Li_2CO_3, Mn_2O_3, $NiCO_3$, TiO_2, and Cr_2O_3 were used as precursors, with the use of 5% excess Li_2CO_3. The precursors were mixed in ethanol and ball milled for 15 h. The mixture was then dried and pelletized. To prepare $Li_{1.2}Mn_{0.4}Ti_{0.4}O_2$, $Li_{1.2}Mn_{0.3}Ti_{0.4}Cr_{0.1}O_2$, and $Li_{1.2}Mn_{0.2}Ti_{0.4}Cr_{0.2}O_2$, the precursor mixtures were heated at 1000 °C, 1000 °C, and 1050 °C for 10 h under argon, respectively. To prepare $Li_{1.2}Ni_{0.2}Ti_{0.6}O_2$ and $Li_{1.2}Ni_{0.15}Ti_{0.55}Cr_{0.1}O_2$, the precursor mixtures were heated at 1000 °C for 3 h in air. To prepare $Li_{1.2}Ni_{0.1}Ti_{0.5}Cr_{0.2}O_2$, the mixture was heated at 1050 °C for 10 h in air.

Electrochemistry. The active material, carbon black (Timcal, SUPER C65), and polytetrafluoroethylene (PTFE, DuPont, Teflon 8A) were mixed at a weight ratio of 70:20:10 to prepare the cathode film. First, 210 mg of the active material and 60 mg of carbon black were mixed and shaker-milled for 1 h in an argon atmosphere using a SPEX 800M mixer, and PTFE was then added to the mixture and manually mixed for 30 min. The three components were rolled

into a thin film inside an argon-filled glove box. The electrolyte used was 1 M $LiPF_6$ in 1:1 (volume ratio) ethylene carbonate (EC) and dimethyl carbonate (DMC) (BASF). Coin cells were assembled using the cathode film, lithium-metal foil, the electrolyte, and separators (Whatman glass microfiber filter) in an argon-filled glove box. The loading density of active material was approximately 3 mg cm^{-2} for each cathode film, and the electrolyte amount was approximately 0.2 mL (4 drops). Galvanostatic cycling tests were performed at room temperature using an Arbin battery tester. GITT measurements were performed by charging/discharging the cell for 270 s at a current density of 200 mA g^{-1} and relaxing for 12 h to reach a quasi-equilibrium state. Electrochemically delithiated/lithiated samples were prepared by charging/discharging the cells at a current density of 20 mA g^{-1}, and the charged/discharged cathode films were collected after washing with DMC in an argon-filled glove box.

Characterization. XRD patterns of the as-prepared materials were collected using a Bruker D8 ADVANCE diffractometer (Cu source) in the 2θ range of 15°–85°. Rietveld refinement was performed using the PANalytical X'Pert HighScore Plus software. TEM was performed using a Titan X at 200 kV. EDS mappings were taken in STEM mode. SEM images were obtained using a Zeiss Gemini Ultra-55 analytical field-emission scanning electron microscope with acceleration voltages of 5–10 kV.

Hard XAS. Mn K-edge, Cr K-edge, Ti K-edge, and Ni K-edge XAS measurements were performed at beamline 20BM at the Advanced Photon Source, Argonne National Laboratory. The measurements were collected in transmission mode using a Si (111) monochromator. Mn foil (6539 eV), Cr foil (5989 eV), Ti foil (4966 eV), or Ni foil (8333 eV) was simultaneously measured during the experiments to calibrate the energy of the individual data set. All the ex-situ samples were sealed between polyimide tapes to avoid air exposure. The XAS spectra were calibrated and

normalized using the Athena software package.[39,40] The background contribution was limited below R_{bkg} = 1.0 using the built-in AUTOBK algorithm. The normalized spectra were converted from energy to wave-vector k and then Fourier transformed from k-space to R-space. The R values should be ~0.3 to 0.4 shorter than the actual distances because the Fourier transform was not phase corrected.[16] The EXAFS of the Cr edge was analyzed using the Artemis software package. The EXAFS fitting was conducted using a Hanning window in k, k^2, and k^3 k-weights simultaneously. The structural models for the fittings were adapted from DFT-calculated structures. The Cr–O and Cr–TM single scattering paths were utilized to fit the octahedral Cr–O and Cr–TM bonds, respectively. To fit the EXAFS spectra with tetrahedral Cr–O contribution, a Cr–O path (1.65 Å) generated by FEFF calculation was used. The amplitude reduction factor S_0^2 was determined by fitting the Cr foil EXAFS spectrum, and the obtained value (0.7) was used for the fits. k^2-weighted EXAFS spectra are displayed in the figures.

RIXS. The RIXS data were collected at the iRIXS endstation at beamline 8.0.1 at the Advanced Light Source, Lawrence Berkeley National Laboratory. The samples were mounted on a 1-inch copper sample holder and transferred from an argon glovebox into the vacuum chamber using a home-made sample transfer kit to avoid any air exposure. Detailed experimental setups and the RIXS data processing have been described previously.[41,42]

DEMS measurements. Custom Swagelok cells were used for the DEMS measurements, as described previously [43–45]. The electrolyte, separators, and anodes used were identical to those used for the coin-cell tests in this study. The loading density of active material was 14 mg cm^{-2} for the cathode film, and the film was backed by stainless steel mesh to provide the appropriate diameter for electrical contact with the customized current collector. The hermetically sealed cells were assembled in an argon-atmosphere glovebox and appropriately attached to the DEMS apparatus to

avoid air exposure. The cells were cycled at a current of 20 mA g^{-1} using a Bio-Logic VSP-Series potentiostat under positive Ar pressure (approximately 1.2 bar). During electrochemical cycling, the gas evolution was monitored using a custom-built DEMS apparatus, as described in a previous report[43].

Computational methods. To evaluate the equilibrium ordering in the multicomponent DRX compounds, we constructed a cluster-expansion Hamiltonian in the configurational space of $LiMnO_2$–$LiCrO_2$–Li_2TiO_3 on a rocksalt lattice. The cluster expansion technique is used to study the configurational thermodynamics of materials in which sites can be occupied by multiple cations, and has been applied to study Li-vacancy configuration in layered materials[46]. As in the $LiMnO_2$–$LiCrO_2$–Li_2TiO_3 system, the cation fcc lattice can be occupied by Li^+–Ti^{4+}–Mn^{3+}–Cr^{3+}. We fit a cluster-expansion model consisting of pair interactions up to 7.1 Å, triplet interactions up to 4 Å, and quadruplet interactions up to 4 Å based on a primitive cell of the rocksalt structure with a = 3 Å. The effective cluster interactions (ECIs) were obtained from ℓ_1-norm regularized linear regression with the best regularization parameter selected to minimize the cross-validation (CV) score.[47,48] Finally, the root-mean squared (RMS) cross-validation errors were converged below 8 meV/atom.

Density functional theory (DFT) calculations were performed using the *Vienna ab initio simulation package* (VASP)[49] using the projector-augmented wave method[50], a plane-wave basis set with an energy cutoff equal to 520 eV, and a reciprocal space discretization of 25 k-points per Å. All the calculations were converged to 10^{-6} eV in total energy for electronic loops and 0.02 eV/Å in interatomic forces for ionic loops. We relied on the Perdew–Burke–Ernzerhof (PBE) generalized gradient approximation exchange-correlation functional with rotationally averaged Hubbard U correction (GGA+U) to compensate for the self-interaction error on all TM atoms except

titanium.[51] The U parameters were obtained from literature, where they were calibrated to TM oxide formation energies (3.9 eV for Mn and 3.5 eV for Cr).[52] The GGA+U computational framework is believed to be reliable in determining the formation enthalpies of similar compounds.[53]

Monte Carlo simulations on these cluster expansion Hamiltonians were performed in a canonical ensemble using Metropolis–Hastings sampling on a 8 × 9 × 10 supercell (1440 atoms) of the primitive unit cell of the rocksalt structure. Percolation analysis was completed on these sampled structures using the *dribble* package.[14]

To compare the formation energies of Cr_{oct} and Cr_{tet}, representative Monte Carlo (MC) structures from equilibrium ensemble sampled at T = 1273K were generated with composition $Li_{1.2}Mn_{0.2}Cr_{0.2}Ti_{0.4}O_{2.0}$ to represent the random arrangement of 120 atoms. All the Li_3Cr clusters in the MC structures were considered for Cr migration because the large electrostatic repulsion[54] between face-sharing tet-Cr and oct-TM prohibits the occupancy of Cr in the tetrahedral site. Starting from the Li_3Cr tetrahedral cluster shown in Supplementary Fig. 13, a tri-vacancy configuration was created by removing the three Li atoms in the Li_3Cr cluster. The energy of the system ($Li_{33}Mn_6Cr_6Ti_{12}O_{60}$) with the Cr atom placed in either the octahedral or tetrahedral site was evaluated. The R2SCAN meta-GGA exchange-correlation functional was used with a reciprocal space discretization of 25 *k*-points per Å. The SCAN functional is believed to better capture charge transfer due to redox, which would improve the accuracy of energetics involving Li removal[55,56]. All the calculations were converged to 10^{-6} eV in total energy for electronic loops and 0.02 eV/Å in interatomic forces for ionic loops.

The nudged elastic band (NEB) method was used to compute Cr migration barriers[57] based on five images along the path from the octahedral to the tetrahedral site. The octahedral and tetrahedral

structures were relaxed with the GGA functional with converge to 10^{-6} eV in total energy for electronic loops and 0.02 eV/Å in interatomic forces for ionic loops. All NEB calculations were performed using GGA without Hubbard-U correction to avoid potential convergence issues associated with electron localization at various atomic centers along the migration path.[58,59]

Data availability

All data generated and analysed during this study are included in the published article and its Supplementary Information. Source data are provided with this paper.

References

1. Kang, K., Meng, Y. S., Bréger, J., Grey, C. P. & Ceder, G. Electrodes with high power and high capacity for rechargeable lithium batteries. *Science (80-.).* **311**, 977–980 (2006).
2. Schougaard, S. B., Bréger, J., Jiang, M., Grey, C. P. & Goodenough, J. B. LiNi0.5+δMn0.5–δO2—A High-Rate, High-Capacity Cathode for Lithium Rechargeable Batteries. *Adv. Mater.* **18**, 905–909 (2006).
3. Julien, C. & Nazri, G. A. Chapter 3 - Intercalation compounds for advanced lithium batteries. in (ed. Singh Nalwa, H. B. T.-H. of A. E. and P. M. and D.) 99–184 (Academic Press, 2001). doi:https://doi.org/10.1016/B978-012513745-4/50083-4
4. Jacobson, A. J. & Nazar, L. F. Intercalation Chemistry. *Encyclopedia of Inorganic and Bioinorganic Chemistry* (2011). doi:https://doi.org/10.1002/9781119951438.eibc0093
5. Wu, F. & Yushin, G. Conversion cathodes for rechargeable lithium and lithium-ion batteries. *Energy Environ. Sci.* **10**, 435–459 (2017).
6. Wiaderek, K. M. *et al.* Comprehensive Insights into the Structural and Chemical Changes in Mixed-Anion FeOF Electrodes by Using Operando PDF and NMR Spectroscopy. *J. Am. Chem. Soc.* **135**, 4070–4078 (2013).
7. Yu, H.-C. *et al.* Designing the next generation high capacity battery electrodes. *Energy Environ. Sci.* **7**, 1760–1768 (2014).
8. Huang, Q. *et al.* Fading Mechanisms and Voltage Hysteresis in FeF2–NiF2 Solid Solution Cathodes for Lithium and Lithium-Ion Batteries. *Small* **15**, 1804670 (2019).
9. Hua, X. *et al.* Comprehensive Study of the CuF2 Conversion Reaction Mechanism in a Lithium Ion Battery. *J. Phys. Chem. C* **118**, 15169–15184 (2014).
10. Bréger, J. *et al.* Effect of High Voltage on the Structure and Electrochemistry of LiNi0.5Mn0.5O2: A Joint Experimental and Theoretical Study. *Chem. Mater.* **18**, 4768–4781 (2006).
11. Li, H. H. *et al.* Changes in the Cation Ordering of Layered O3 LixNi0.5Mn0.5O2 during

Electrochemical Cycling to High Voltages: An Electron Diffraction Study. *Chem. Mater.* **19**, 2551–2565 (2007).
12. Jones, C. D. W., Rossen, E. & Dahn, J. R. Structure and electrochemistry of LixCryCo1−yO2. *Solid State Ionics* **68**, 65–69 (1994).
13. Lyu, Y. *et al.* Atomic insight into electrochemical inactivity of lithium chromate (LiCrO2): Irreversible migration of chromium into lithium layers in surface regions. *J. Power Sources* **273**, 1218–1225 (2015).
14. Lee, J. *et al.* Unlocking the potential of cation-disordered oxides for rechargeable lithium batteries. *Science (80-.).* **343**, 519–522 (2014).
15. Clément, R. J., Lun, Z. & Ceder, G. Cation-disordered rocksalt transition metal oxides and oxyfluorides for high energy lithium-ion cathodes. *Energy Environ. Sci.* **13**, 345–373 (2020).
16. Balasubramanian, M., McBreen, J., Davidson, I. J., Whitfield, P. S. & Kargina, I. In Situ X-Ray Absorption Study of a Layered Manganese-Chromium Oxide-Based Cathode Material. *J. Electrochem. Soc.* **149**, A176–A184 (2002).
17. Yang, W. & Devereaux, T. P. Anionic and cationic redox and interfaces in batteries: Advances from soft X-ray absorption spectroscopy to resonant inelastic scattering. *J. Power Sources* **389**, 188–197 (2018).
18. Dai, K. *et al.* High Reversibility of Lattice Oxygen Redox Quantified by Direct Bulk Probes of Both Anionic and Cationic Redox Reactions. *Joule* **3**, 518–541 (2019).
19. Li, N. *et al.* Correlating the phase evolution and anionic redox in Co-Free Ni-Rich layered oxide cathodes. *Nano Energy* **78**, 105365 (2020).
20. Papp, J. K. *et al.* A comparison of high voltage outgassing of LiCoO2, LiNiO2, and Li2MnO3 layered Li-ion cathode materials. *Electrochim. Acta* **368**, 137505 (2021).
21. Renfrew, S. E. & McCloskey, B. D. Residual Lithium Carbonate Predominantly Accounts for First Cycle CO2 and CO Outgassing of Li-Stoichiometric and Li-Rich Layered Transition-Metal Oxides. *J. Am. Chem. Soc.* **139**, 17853–17860 (2017).
22. Renfrew, S. E. & McCloskey, B. D. Quantification of Surface Oxygen Depletion and Solid Carbonate Evolution on the First Cycle of LiNi0.6Mn0.2Co0.2O2 Electrodes. *ACS Appl. Energy Mater.* **2**, 3762–3772 (2019).
23. Van der Ven, A. & Ceder, G. Lithium diffusion mechanisms in layered intercalation compounds. *J. Power Sources* **97–98**, 529–531 (2001).
24. Van der Ven, A. Lithium Diffusion in Layered Li[sub x]CoO[sub 2]. *Electrochem. Solid-State Lett.* **3**, 301 (1999).
25. Urban, A., Lee, J. & Ceder, G. The Configurational Space of Rocksalt-Type Oxides for High-Capacity Lithium Battery Electrodes. *Adv. Energy Mater.* **4**, 1400478 (2014).
26. Reed, J. & Ceder, G. Role of Electronic Structure in the Susceptibility of Metastable Transition-Metal Oxide Structures to Transformation. *Chem. Rev.* **104**, 4513–4534 (2004).
27. Shannon, R. D. Revised effective ionic radii and systematic studies of interatomic distances in halides and chalcogenides. *Acta Crystallogr. Sect. A* **32**, 751–767 (1976).
28. Ji, H. *et al.* Hidden structural and chemical order controls lithium transport in cation-disordered oxides for rechargeable batteries. *Nat. Commun.* **10**, 592 (2019).
29. Nakajima, M. & Yabuuchi, N. Lithium-Excess Cation-Disordered Rocksalt-Type Oxide with Nanoscale Phase Segregation: Li1.25Nb0.25V0.5O2. *Chem. Mater.* **29**, 6927–6935 (2017).
30. Zhu, Z. *et al.* Gradient Li-rich oxide cathode particles immunized against oxygen release

by a molten salt treatment. *Nat. Energy* **4**, 1049–1058 (2019).
31. Wang, Y., Yang, Z., Qian, Y., Gu, L. & Zhou, H. New Insights into Improving Rate Performance of Lithium-Rich Cathode Material. *Adv. Mater.* **27**, 3915–3920 (2015).
32. Shi, J.-L. *et al.* High-Capacity Cathode Material with High Voltage for Li-Ion Batteries. *Adv. Mater.* **30**, 1705575 (2018).
33. Li, X. *et al.* A New Type of Li-Rich Rock-Salt Oxide Li2Ni1/3Ru2/3O3 with Reversible Anionic Redox Chemistry. *Adv. Mater.* **31**, 1807825 (2019).
34. Hong, J. *et al.* Metal–oxygen decoordination stabilizes anion redox in Li-rich oxides. *Nat. Mater.* **18**, 256–265 (2019).
35. Kang, K. & Ceder, G. Factors that affect Li mobility in layered lithium transition metal oxides. *Phys. Rev. B* **74**, 94105 (2006).
36. Sathiya, M. *et al.* Origin of voltage decay in high-capacity layered oxide electrodes. *Nat. Mater.* **14**, 230–238 (2015).
37. Bréger, J., Kang, K., Cabana, J., Ceder, G. & Grey, C. P. NMR, PDF and RMC study of the positive electrode material Li(Ni0.5Mn0.5)O2 synthesized by ion-exchange methods. *J. Mater. Chem.* **17**, 3167–3174 (2007).
38. Sun, X., Duffort, V., Mehdi, B. L., Browning, N. D. & Nazar, L. F. Investigation of the Mechanism of Mg Insertion in Birnessite in Nonaqueous and Aqueous Rechargeable Mg-Ion Batteries. *Chem. Mater.* **28**, 534–542 (2016).
39. Ravel, B. & Newville, M. ATHENA, ARTEMIS, HEPHAESTUS: data analysis for X-ray absorption spectroscopy using IFEFFIT. *J. Synchrotron Radiat.* **12**, 537–541 (2005).
40. Ravel, B. & Newville, M. ATHENA and ARTEMIS Interactive Graphical Data Analysisusing IFEFFIT. *Phys. Scr.* 1007 (2005). doi:10.1238/physica.topical.115a01007
41. Qiao, R. *et al.* High-efficiency in situ resonant inelastic x-ray scattering (iRIXS) endstation at the Advanced Light Source. *Rev. Sci. Instrum.* **88**, 33106 (2017).
42. AU - Wu, J. *et al.* Elemental-sensitive Detection of the Chemistry in Batteries through Soft X-ray Absorption Spectroscopy and Resonant Inelastic X-ray Scattering. *JoVE* e57415 (2018). doi:doi:10.3791/57415
43. Mccloskey, B. D., Bethune, D. S., Shelby, R. M., Girishkumar, G. & Luntz, A. C. Solvents ' Critical Role in Nonaqueous Lithium-Oxygen Battery Electrochemistry. *J. Phys. Chem. Lett.* 1161–1166 (2011). doi:10.1021/jz200352v
44. Mccloskey, B. D. *et al.* Combining accurate O2 and Li2O2 assays to separate discharge and charge stability limitations in nonaqueous Li-O 2 Batteries. *J. Phys. Chem. Lett.* **4**, 2989–2993 (2013).
45. McCloskey, B. D. *et al.* Twin problems of interfacial carbonate formation in nonaqueous Li-O 2 batteries. *J. Phys. Chem. Lett.* **3**, 997–1001 (2012).
46. Van der Ven, A., Aydinol, M. K., Ceder, G., Kresse, G. & Hafner, J. First-principles investigation of phase stability in ${\mathrm{Li}}_{x}{\mathrm{CoO}}_{2}$. *Phys. Rev. B* **58**, 2975–2987 (1998).
47. van de Walle, A. Multicomponent multisublattice alloys, nonconfigurational entropy and other additions to the Alloy Theoretic Automated Toolkit. *Calphad* **33**, 266–278 (2009).
48. Nelson, L. J., Hart, G. L. W., Zhou, F. & Ozoliņš, V. Compressive sensing as a paradigm for building physics models. *Phys. Rev. B* **87**, 35125 (2013).
49. Kresse, G. & Furthmüller, J. Efficiency of ab-initio total energy calculations for metals and semiconductors using a plane-wave basis set. *Comput. Mater. Sci.* **6**, 15–50 (1996).
50. Kresse, G. & Joubert, D. From ultrasoft pseudopotentials to the projector augmented-wave

method. *Phys. Rev. B* **59**, 1758–1775 (1999).
51. Perdew, J. P., Burke, K. & Ernzerhof, M. Generalized Gradient Approximation Made Simple. *Phys. Rev. Lett.* **77**, 3865–3868 (1996).
52. Wang, L., Maxisch, T. & Ceder, G. Oxidation energies of transition metal oxides within the $\mathrm{GGA}+\mathrm{U}$ framework. *Phys. Rev. B* **73**, 195107 (2006).
53. Jain, A. *et al.* Formation enthalpies by mixing GGA and GGA $+$ U calculations. *Phys. Rev. B* **84**, 45115 (2011).
54. Reed, J., Ceder, G. & Van Der Ven, A. Layered-to-Spinel Phase Transition in Li[sub x]MnO[sub 2]. *Electrochem. Solid-State Lett.* **4**, A78 (2001).
55. Sun, J., Ruzsinszky, A. & Perdew, J. P. Strongly Constrained and Appropriately Normed Semilocal Density Functional. *Phys. Rev. Lett.* **115**, 36402 (2015).
56. Kitchaev, D. A. *et al.* Energetics of ${\mathrm{MnO}}_{2}$ polymorphs in density functional theory. *Phys. Rev. B* **93**, 45132 (2016).
57. Henkelman, G. & Jónsson, H. Improved tangent estimate in the nudged elastic band method for finding minimum energy paths and saddle points. *J. Chem. Phys.* **113**, 9978–9985 (2000).
58. Urban, A., Seo, D.-H. & Ceder, G. Computational understanding of Li-ion batteries. *npj Comput. Mater.* **2**, 16002 (2016).
59. Asari, Y., Suwa, Y. & Hamada, T. Formation and diffusion of vacancy-polaron complex in olivine-type LiMnPO${}_{4}$ and LiFePO${}_{4}$. *Phys. Rev. B* **84**, 134113 (2011).

Acknowledgements

This work was supported by the Assistant Secretary for Energy Efficiency and Renewable Energy, Vehicle Technologies Office, under the Applied Battery Materials Program, of the U.S. Department of Energy under Contract No. DE-AC02-05CH11231. The XAS measurements were performed at the Advanced Photon Source at Argonne National Laboratory, which is supported by the U.S. Department of Energy under Contract No. DE-AC02-06CH11357. Work at the Molecular Foundry was supported by the Office of Science, Office of Basic Energy Sciences, of the U.S. Department of Energy under Contract No. DE-AC02-05CH11231. The computational analysis was performed using computational resources sponsored by the Department of Energy's Office of Energy Efficiency and Renewable Energy and located at the National Renewable Energy Laboratory as well as computational resources provided by the Extreme Science and Engineering Discovery Environment (XSEDE), supported by National Science Foundation grant number

ACI1053575, and the National Energy Research Scientific Computing Center (NERSC), a DOE Office of Science User Facility supported by the Office of Science and the U.S. Department of Energy under Contract No. DE-AC02-05CH11231. The authors thank Dr. Hyunchul Kim and Zhengyan Lun for assistance with the XAS measurements.

Author contributions

J.H. and G.C. planned the project. G.C. supervised all aspects of the research. J.H. synthesized, characterized, and electrochemically tested the proposed materials. J.H. also analyzed the ex-situ XAS data with help from M.H. P.Z. performed the theoretical calculations and analyzed the results. D.K. performed the TEM characterization. Y.H. collected and analyzed the RIXS data with W.Y. M.C. collected and analyzed the DEMS data with input from B.D.M. Y.T. performed the SEM characterization. The manuscript was written by J.H. and G.C. and was revised by the other co-authors. All the authors contributed to discussions.

Competing interests

The authors declare no competing interests.

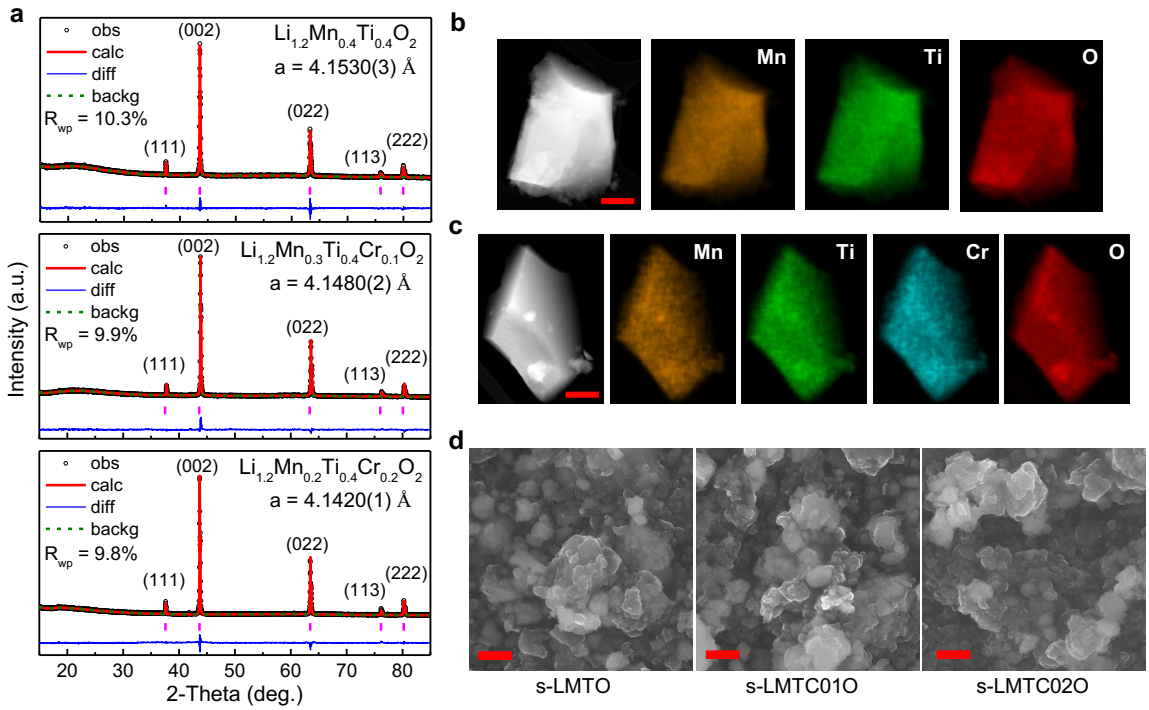

Fig. 1 | Structure characterization of $Li_{1.2}Mn_{0.4-x}Ti_{0.4}Cr_xO_2$. (a) XRD patterns and refinement results of $Li_{1.2}Mn_{0.4}Ti_{0.4}O_2$ (LMTO), $Li_{1.2}Mn_{0.3}Ti_{0.4}Cr_{0.1}O_2$ (LMTC01O), and $Li_{1.2}Mn_{0.2}Ti_{0.4}Cr_{0.2}O_2$ (LMTC02O). Refinement was performed using space group Fm-3m. Bragg positions are indicated as purple vertical bars. TEM images and EDS mappings of (b) LMTO and (c) LMTC02O. Scale bar: 300 nm. (d) SEM images of shaker-milled LMTO (s-LMTO), LMTC01O (s-LMTC01O), and LMTC02O (s-LMTC02O). Scale bar: 500 nm.

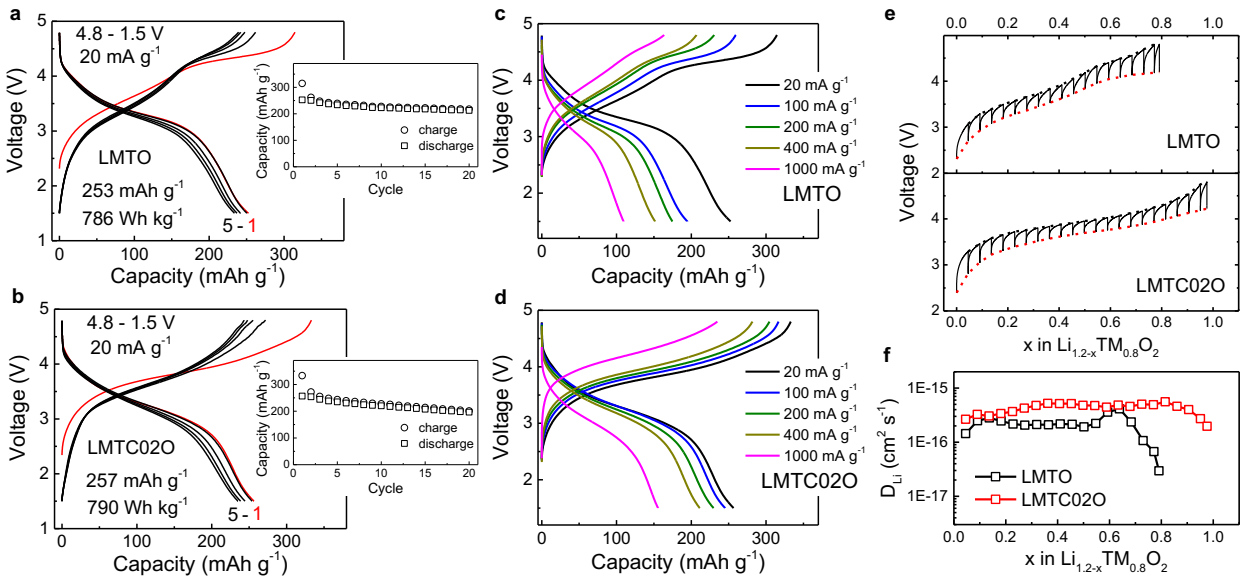

Fig. 2 | Electrochemistry of $Li_{1.2}Mn_{0.4-x}Ti_{0.4}Cr_xO_2$ at room temperature. Voltage profiles of (a) LMTO and (b) LMTC02O at 20 mA g^{-1} in the voltage window of 4.8–1.5 V. The insets show the capacity retention of the samples over 20 cycles. First-cycle voltage profiles of (c) LMTO and (d) LMTC02O at different current densities. (e) Voltage profiles of LMTO and LMTC02O under galvanostatic intermittent titration technique (GITT) mode. (f) Apparent Li diffusion coefficients of LMTO and LMTC02O calculated from the GITT results.

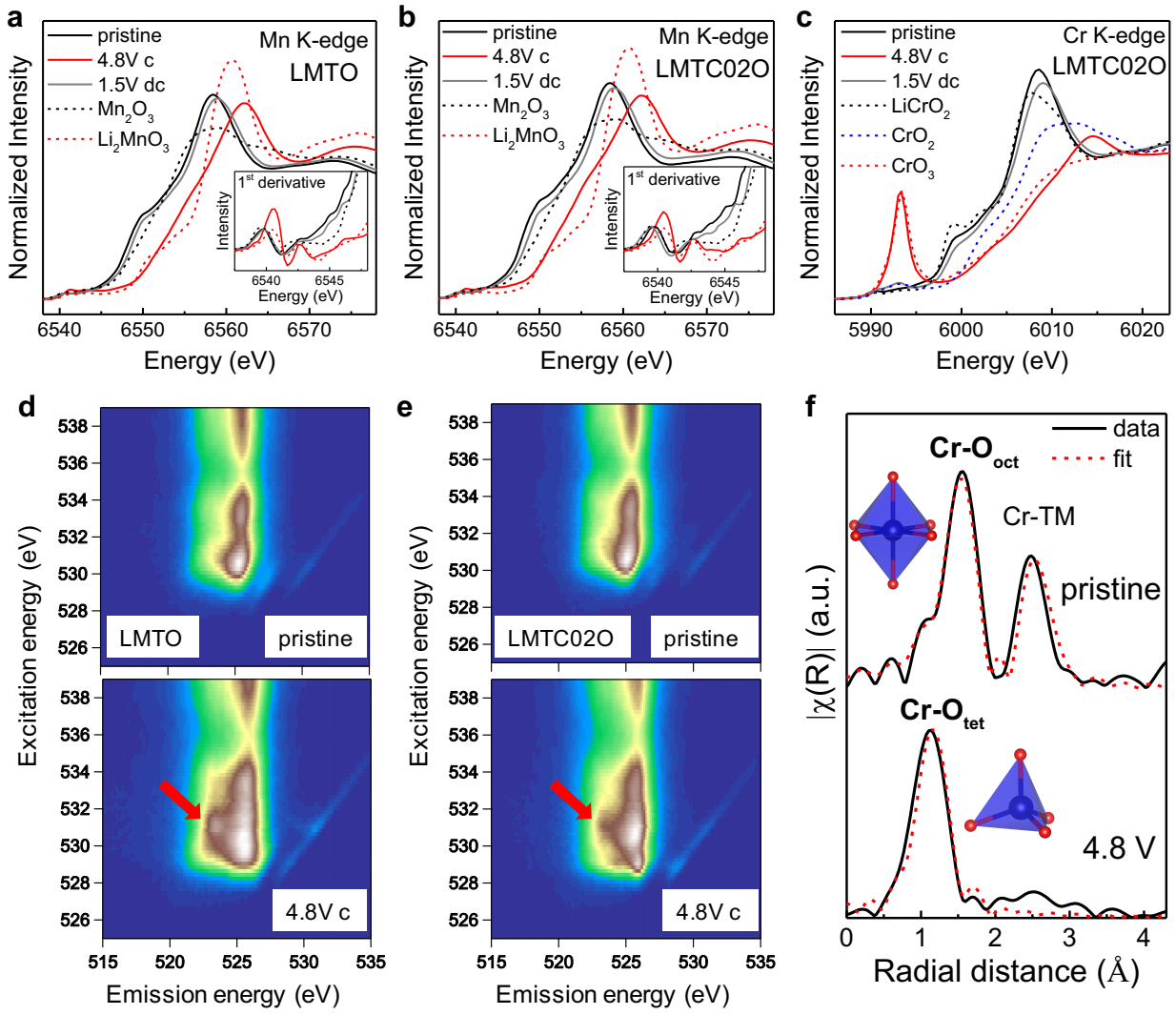

Fig. 3 | Redox mechanism and structural change of $Li_{1.2}Mn_{0.4-x}Ti_{0.4}Cr_xO_2$. Mn K-edge XANES spectra of (a) LMTO and (b) LMTC02O in pristine, 4.8-V-charged, and 1.5-V-discharged state. The spectra of Mn_2O_3 and Li_2MnO_3 standards are plotted as dashed lines. The insets show the first derivatives of normalized absorbance in the pre-edge regions of the Mn K-edge XANES spectra. (c) Cr K-edge XANES spectra of LMTC02O in pristine, 4.8-V-charged, and 1.5-V-discharged state. The spectra of $LiCrO_2$, CrO_2, and CrO_3 standards are plotted as dashed lines. O K-edge mRIXS of (d) LMTO and (e) LMTC02O in pristine and 4.8-V-charged state. (f) Fitted Cr K-edge EXAFS spectra of LMTC02O in pristine and 4.8-V-charged state. The fitting was

performed in the radial distance of 1 to 3 Å using Cr–O and Cr–TM single scattering paths. The peaks at ~1.0, ~1.5, and ~2.5 Å correspond to the tetrahedral Cr–O ($Cr–O_{tet}$), octahedral Cr–O ($Cr–O_{oct}$), and Cr–TM coordination, respectively. The insets show the octahedral CrO_6 and tetrahedral CrO_4 coordination.

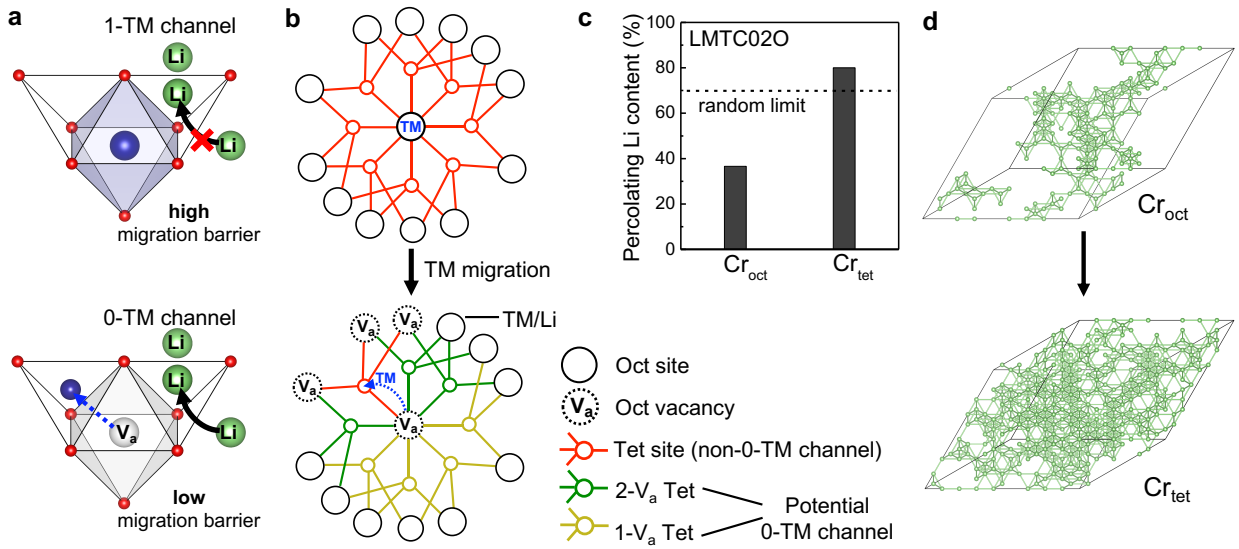

Fig. 4 | Effect of TM migration on Li kinetics. (a) Illustration of a TMO_6 octahedron with two face-sharing tetrahedral sites. Migration of the TM from the octahedron transforms a 1-TM channel (a tetrahedral site with one face-sharing octahedral TM) into a 0-TM channel (b) Illustration of Li pathway availability in a rocksalt-type structure before and after TM migration. The structure shows an octahedral TM is connected to eight tetrahedral sites. The presence of the TM in the octahedral site makes all eight tetrahedral sites non-0-TM channels (red circle). After the TM migrates to a tetrahedral site, the other seven tetrahedral sites become potential 0-TM channels (green or yellow circle), depending on the cations in the other nearby octahedra. (c) Calculated percolating Li content via 0-TM channel in LMTC02O when Cr occupies octahedral sites (Cr_{oct}) in the pristine state and tetrahedral sites (Cr_{tet}) after possible migration. The dotted line shows the percolating Li content via the 0-TM channel in the random structure limit. (d) Representative Monte Carlo simulated structures for LMTC02O with octahedral Cr and tetrahedral Cr. Li are plotted with green spheres, and 0-TM connected Li are bridged with green lines.

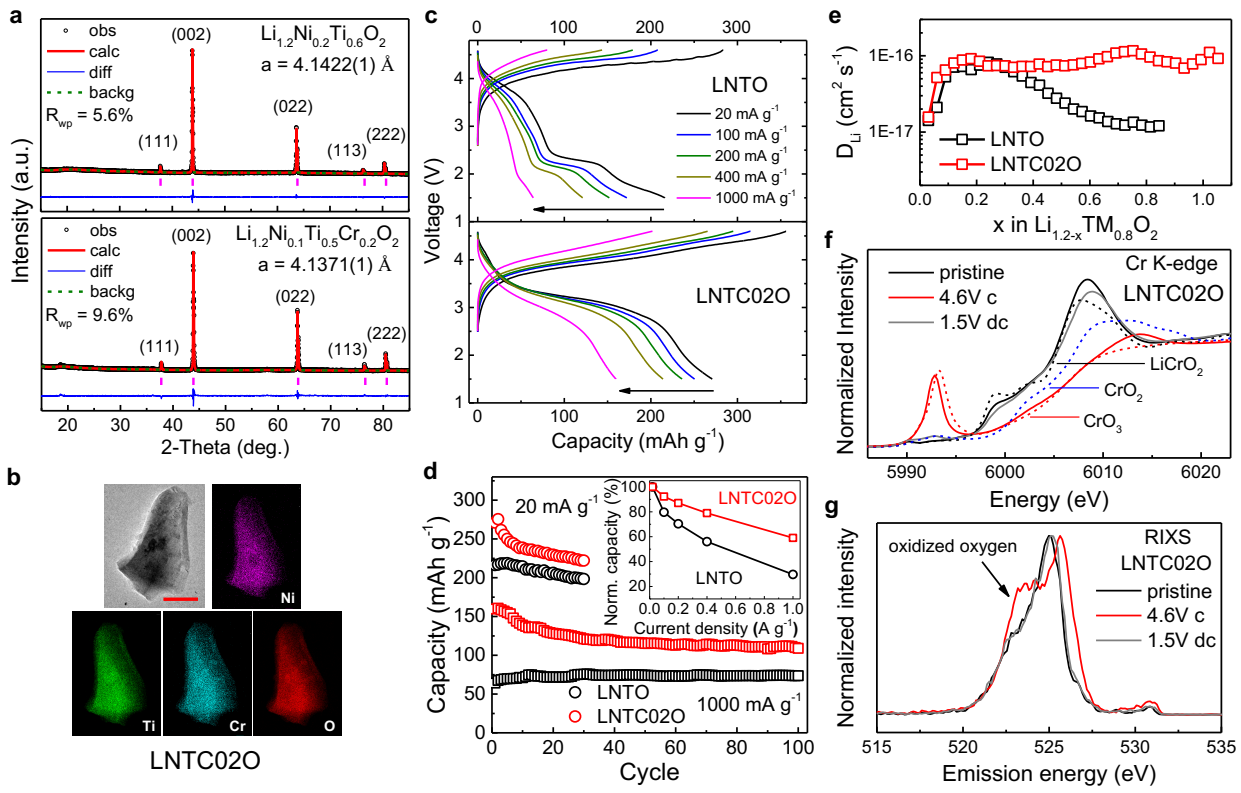

Fig. 5 | Structural characterization and electrochemistry of $Li_{1.2}Ni_{0.2-x}Ti_{0.6-x}Cr_{2x}O_2$. (a) XRD patterns and refinement results for $Li_{1.2}Ni_{0.2}Ti_{0.6}O_2$ (LNTO) and $Li_{1.2}Ni_{0.1}Ti_{0.5}Cr_{0.2}O_2$ (LNTC02O). Refinement was performed using space group Fm-3m. Bragg positions are indicated as purple vertical bars. (b) TEM image and EDS mapping of a LNTC02O particle. Scale bar: 200 nm. (c) First-cycle voltage profiles of LNTO and LNTC02O at different current densities in the voltage window of 4.6–1.5 V. (d) Capacity retention of LNTO and LNTC02O at 20 and 1000 mA g^{-1} in the voltage window of 4.6–1.5 V. The inset shows the normalized capacity as a function of current density. (e) Apparent lithium-ion diffusion coefficients of LNTO and LNTC02O calculated from the GITT results. (f) Cr K-edge XANES spectra of LNTC02O in pristine, 4.6-V-charged, and 1.5-V-discharged state. (g) O L-edge RIXS spectra of LNTC02O collected at an excitation energy of 531 eV. The peak at an emission energy of 523.7 eV is a characteristic feature of oxidized oxygen.